mathematics

Article

Coupled Inductor-Based ZVS Interleaved Buck Converter with Optimal Coupling Coefficient and Fully Digital BCM Control

Jingtao Xu [1], Xilin Chen [1] and Xiaochao Hou [2,*]

[1] School of Traffic & Transportation Engineering, Central South University, Changsha 410075, China; xjt4ugo@csu.edu.cn (J.X.); 254212056@csu.edu.cn (X.C.)
[2] School of Electronic Information, Central South University, Changsha 410075, China
* Correspondence: houxc10@csu.edu.cn

Abstract

In this paper, a coupled-inductor-based interleaved Buck converter is presented. By employing a negatively coupled inductor, the proposed topology reduces magnetic component number and improves dynamic response. Operating in boundary conduction mode (BCM), the proposed converter can achieve zero-voltage switching (ZVS) under a wide voltage and load range. The control strategy is fully digital, allowing the switching frequency to be adaptively adjusted without the need for a zero-crossing detection (ZCD) circuit. Furthermore, an optimal coupling coefficient design is proposed, which minimizes the frequency adjustment range. In addition, the design process for a coupled inductor with an interleaved winding structure is introduced in detail. Finally, a 300 W experimental prototype is built, the experimental results of which demonstrate its effectiveness and feasibility.

Keywords: interleaved buck converter; coupled inductor; optimal design; BCM; ZVS

MSC: 93C62

1. Introduction

DC/DC converters are widely used in industrial applications such as renewable energy generation and energy storage systems [1,2]. Among them, the Buck and Boost converters are commonly used due to their simple structures [3,4]. As the switching frequency increases, in order to reduce switching losses, ZVS soft switching needs to be adopted. Generally, ZVS can be achieved by adding auxiliary clamping circuits [5,6]. In addition, the zero-voltage transition (ZVT) converter, which can also achieve ZVS operation and effectively reduce switching losses, is implemented [7]. However, the reliability of the system is reduced because of the complexity of the driver circuit and control strategy. In [8,9], the addition of auxiliary capacitors or inductors provides additional current paths to achieve ZVS at a fixed switching frequency. Moreover, adding resonant tanks can allow quasi resonant converters to achieve ZVS operation [10,11]. However, among these types of converters, the presence of additional passive components will still increase hardware costs.

Buck and Boost converters operating in BCM can achieve ZVS without additional auxiliary components [12,13]. ZVS can be achieved by employing a smaller filtering inductor and higher current ripple. However, when the operating conditions change, a higher switching frequency will result in a loss of ZVS, while a lower switching frequency

Check for updates

Academic Editors: Nattha Jindapetch and Hiroshi Saito

Received: 29 December 2025
Revised: 18 January 2026
Accepted: 24 January 2026
Published: 12 February 2026

will generate higher circulating current. Therefore, it is necessary to accurately adjust the switching frequency according to different voltages and loads to maintain BCM operation. Adding a zero-crossing detection circuit (ZCD) can achieve BCM operation with good response speed [14,15]. However, ZCD circuits are more sensitive to sampling noise. In addition, high-bandwidth sensors and sampling circuits may also increase hardware costs. In order to simplify hardware circuit design, digital control methods for BCM are studied [16–18]. Under digital control, the switching frequency is calculated based on the average value of the voltage and current, effectively reducing the interference of sampling noise.

In addition, compared with a single-phase DC/DC converter, the interleaved DC/DC converter can achieve higher power capacity and lower current ripple [19]. However, two bulky separated inductors will reduce the total power density. In order to improve the power density, the coupled inductor can be adopted to achieve the integration of magnetic components [20–22]. Nevertheless, the optimization design of coupling coefficient is rarely discussed. Generally, there are two types of coupled inductor: the positively coupled inductor and negatively coupled inductor. Compared with the positively coupled inductor, the negatively coupled inductor can reduce current ripple and improve dynamic performance [23]. However, in the coupled-inductor-based interleaved DC/DC converter, the inductance parameters and the inductor current modes become more complex. During one switching cycle, the inductor current may have multiple operating modes. Hence, the design of coupled inductors and the control of ZVS operation are more challenging.

On the other hand, under BCM modulation, the switching frequency needs to be adjusted in a wide range at different working voltages. The wide frequency range will bring challenges to the design of magnetic components and driving circuits. Therefore, it is necessary to limit the switching frequency through optimized design.

In this paper, a coupled inductor-based interleaved Buck converter with fully digital control and optimal coupling coefficient is proposed, which has two main advantages as follows:

(1) Compared with traditional interleaved parallel DC/DC converters, the proposed optimal coupling coefficient design minimizes the switching frequency range. This characteristic is advantageous for the design of magnetic components and drive circuits, as it can simultaneously reduce switching and magnetic losses.
(2) The coupled inductor current has multiple stages within one switching cycle. In this regard, a unified equation for adjusting the switching frequency has been proposed, and digital BCM control can be achieved. Furthermore, only the average values of voltage and current need to be sampled.

2. Working Principle and Characteristic Analysis

2.1. Steady State Analysis

The interleaved Buck converter with negatively coupled inductor is shown in Figure 1. M is mutual inductance. L_1 and L_2 are self-inductance, and $L_1 = L_2 = L$. The input voltage is V_i, and the output voltage is V_o. The duty cycle of S_1 and S_3 is defined as D. The MOSFETs of each bridge operate complementarily, and the two bridges operate with a 180 degree phase difference.

The two winding currents of the coupled inductor are defined as i_{L1} and i_{L2}. The flow from the midpoint of the bridge to the output side is defined as positive. The voltages of the two inductor windings are v_{L1} and v_{L2}, respectively, which can be expressed in (1).

$$\begin{cases} v_{L1} = L_1 \frac{di_{L1}}{dt} + M \frac{di_{L2}}{dt} \\ v_{L2} = L_2 \frac{di_{L2}}{dt} + M \frac{di_{L1}}{dt} \end{cases} \tag{1}$$

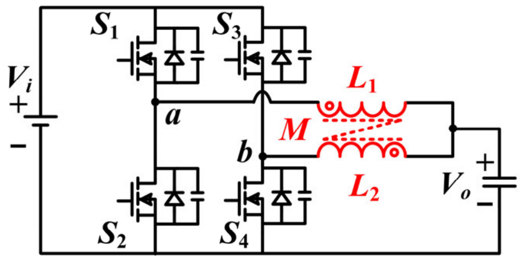

Figure 1. Interleaved Buck converter with negatively coupled inductor.

Because the self-inductance of the two windings is equal (L_1 = L_2 = L), (1) can be derived as

$$Lv_{L1} - Mv_{L2} = (L^2 - M^2) \cdot \frac{di_{L1}}{dt} \tag{2}$$

α is defined as coupling coefficient (α = M/L). (2) can be written as

$$(v_{L1} - \alpha \cdot v_{L2}) = \left(1 - \alpha^2\right) \cdot L \cdot \frac{di_{L1}}{dt} \tag{3}$$

When the relationship between v_{L1} and v_{L2} is determined, according to the definition of the inductance state equation, (3) can be rewritten as

$$v_{L1} = L_{eq} \cdot \frac{di_{L1}}{dt} \tag{4}$$

Because the relationship between v_{L1} and v_{L2} is not constant in a period, the equivalent inductance value L_{eq} will also change at different stages. According to the principle of volt-second balance, V_o is equal to $V_i \times D$. Hence, the relation between v_{L1} and v_{L2} can be expressed as

$$\left\{\begin{array}{l} \left\{\begin{array}{l} v_{L1} = V_i - V_o \\ v_{L2} = -V_o \end{array}\right. \Rightarrow v_{L2} = -\frac{D}{1-D} v_{L1} \\ \left\{\begin{array}{l} \left\{\begin{array}{l} v_{L1} = V_i - V_o \\ v_{L2} = V_i - V_o \end{array}\right. \\ \text{or} \left\{\begin{array}{l} v_{L1} = -V_o \\ v_{L2} = -V_o \end{array}\right. \end{array}\right. \Rightarrow v_{L2} = v_{L1} \\ \left\{\begin{array}{l} v_{L1} = -V_o \\ v_{L2} = V_i - V_o \end{array}\right. \Rightarrow v_{L2} = -\frac{1-D}{D} v_{L1} \end{array}\right. \tag{5}$$

The voltage and current waveforms of the three different conditions during a switching cycle are shown in Figure 2. It can be seen that, during a switching cycle, the inductor current operates in multiple stages.

The first type of equivalent inductance L_{eq1} is shown in area 1, when v_{L1} is equal to $V_i - V_o$ and v_{L2} is equal to $-V_o$. The second type of equivalent inductance L_{eq2} is shown in area 2, when v_{L1} is equal to v_{L2}. The third type of equivalent inductance L_{eq3} is shown in area 3, when v_{L1} is equal to $-V_o$ and v_{L2} is equal to $V_i - V_o$. The three equivalent inductances are listed in Table 1, respectively.

Table 1. Equivalent Inductance.

L_{eq1}	L_{eq2}	L_{eq3}
$\frac{L(1-\alpha^2)}{1+\frac{\alpha D}{1-D}}$	$L(1+\alpha)$	$\frac{L(1-\alpha^2)}{1+\frac{\alpha(1-D)}{D}}$

https://doi.org/10.3390/math14040643

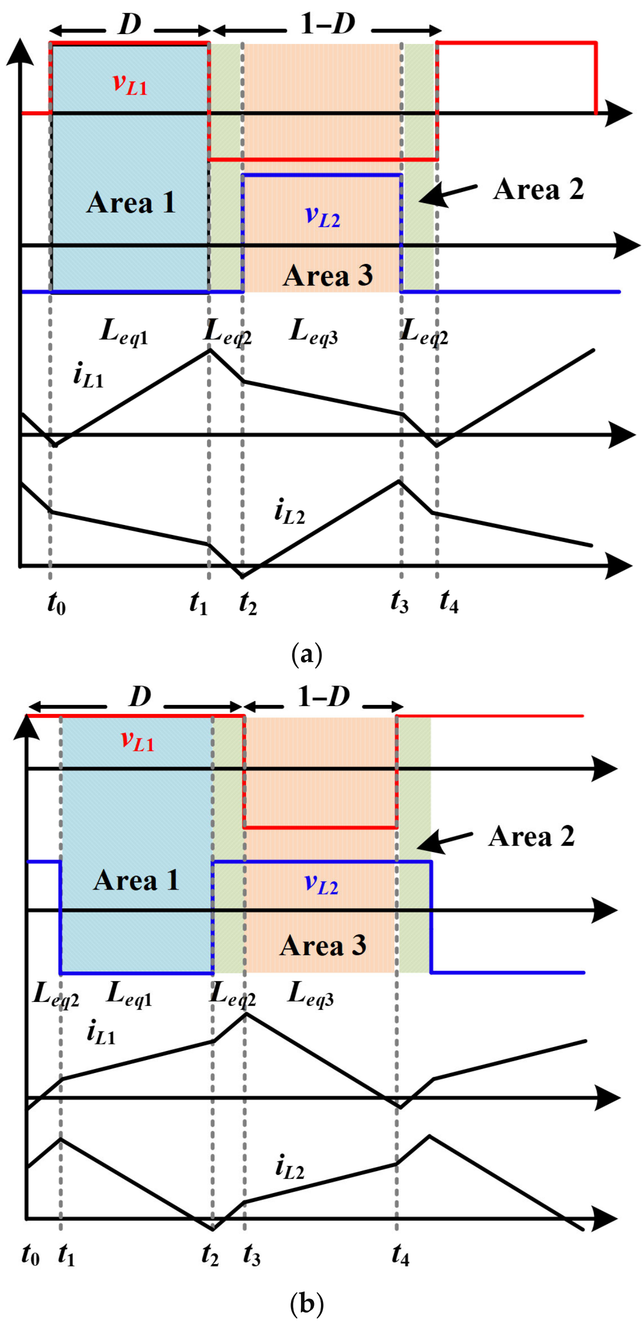

Figure 2. Voltage and current waveforms of steady state. (**a**) $D < 0.5$. (**b**) $D > 0.5$.

2.2. Dynamic Analysis

The dynamic process waveforms are shown in Figure 3. The black dashed line represents the inductor current of the dynamic process. The duty cycle difference is defined as ΔD. During one switching cycle, the current difference Δi_L can be divided into five parts, which can be expressed as

$$\begin{cases} t_0 \sim t_1 : \Delta i_{L1} = (\frac{V_i - V_o}{L_{eq2}} + \frac{V_o}{L_{eq3}})\frac{\Delta D}{f_s} \\ t_1 \sim t_2 : \Delta i_{L2} = (\frac{-V_o}{L_{eq3}} + \frac{V_o}{L_{eq3}})\frac{1-D-\Delta D}{f} = 0 \\ t_2 \sim t_3 : \Delta i_{L3} = (\frac{V_i - V_o}{L_{eq2}} - \frac{V_i - V_o}{L_{eq2}})\frac{D-0.5}{f} = 0 \\ t_3 \sim t_4 : \Delta i_{L4} = (\frac{V_i - V_o}{L_{eq2}} - \frac{V_i - V_o}{L_{eq1}})\frac{\Delta D}{f_s} \\ t_4 \sim t_5 : \Delta i_{L5} = (\frac{V_i - V_o}{L_{eq1}} - \frac{V_i - V_o}{L_{eq1}})\frac{D-0.5}{f} = 0 \end{cases} \tag{6}$$

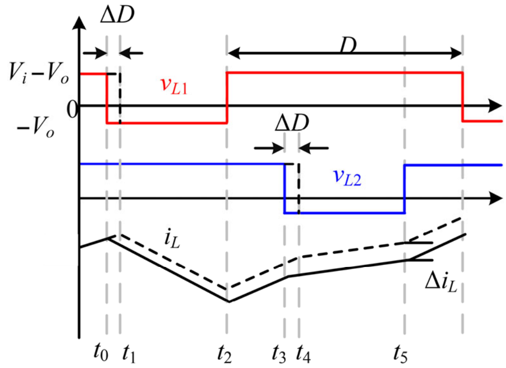

Figure 3. Dynamic process waveforms.

By summing Equation (6), the inductor current difference after one switching cycle can be calculated as

$$\Delta i_L = \sum_{k=1}^{5} \Delta i_k = \left(2 \cdot \frac{V_i - V_o}{L_{eq2}} - \frac{V_i - V_o}{L_{eq1}} + \frac{V_o}{L_{eq3}}\right) \frac{\Delta D}{f_s} \tag{7}$$

The steady-state inductor current satisfies the volt second balance principle, hence the current difference within one switching cycle is equal to zero, which can be expressed as

$$(1-D)\frac{-V_o}{L_{eq3}} + [D-(1-D)]\frac{V_i - V_o}{L_{eq2}} + (1-D)\frac{V_i - V_o}{L_{eq1}} = 0 \tag{8}$$

Finally, combining (7) and (8), the dynamic process inductor current state equation can be derived as

$$\begin{array}{l} \Delta i_L = \frac{1}{1-D} \cdot \frac{V_i - V_o}{L_{eq2}} \cdot \frac{\Delta D}{f_s} \\ \Rightarrow \Delta i_L = \frac{V_i}{L_{eq2}} \cdot \frac{\Delta D}{f_s} \\ \Rightarrow L_{eq2} \cdot \frac{\Delta i_L}{\Delta t} = V_i \end{array} \tag{9}$$

where L_{eq2} is the equivalent inductance when v_{L1} is equal to v_{L2}.

According to (9), it can be seen that the response speed of inductor current is inversely proportional to L_{eq2}. When the coupling coefficient is less than zero, the equivalent inductance L_{eq2} will decrease relative to self-inductance L. Therefore, the interleaved Buck converter with negatively coupled inductor has a higher current response speed.

2.3. ZVS Analysis

For the coupled inductor-based interleaved Buck converter, the calculation of ZVS conditions will be more complex because the inductor current operates in multiple different modes. In this paper, the conditions of ZVS will be unified and easily implemented in digital processors.

The equivalent circuit modes and operating waveforms of ZVS are shown in Figure 4. For S_2, during the dead time at t_1, i_{L1} must be greater than zero, which will flow through the body diode of S_2, as shown in Figure 4b. Therefore, S_2 must achieve ZVS at any voltage and power. For S_1, in order to achieve ZVS, the inductor current needs to be reversed within one switching cycle, as shown in Figure 4c. Therefore, the peak-to-peak value of the inductor current I_{pp} needs to be higher than twice the average value I_{ave}. Hence, it is more difficult to achieve ZVS under full load.

Under BCM, I_{pp} is approximately equal to $2 \times I_{ave}$. This condition can achieve ZVS and reduce circulating current. Therefore, it is necessary to calculate the appropriate switching frequency based on I_{ave}.

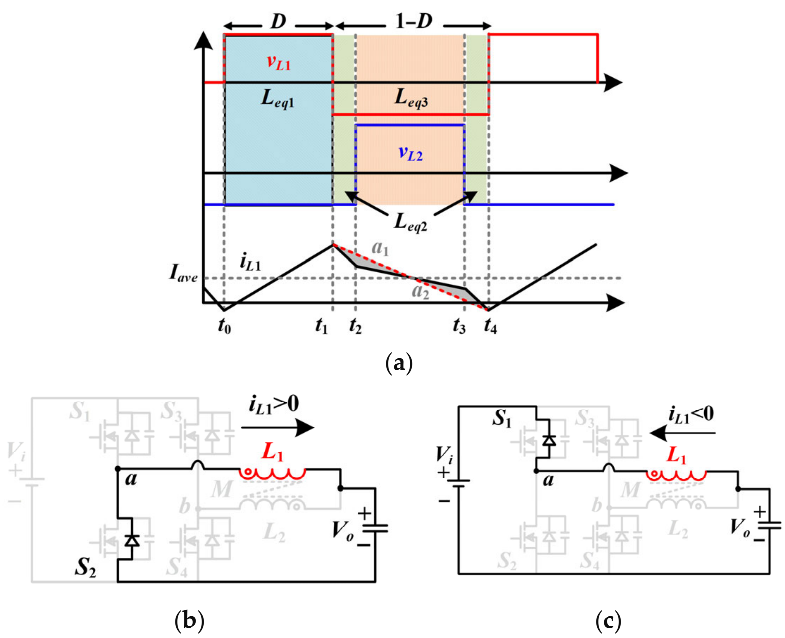

Figure 4. ZVS operation. (**a**) ZVS waveforms. (**b**) ZVS operation equivalent circuit of S_2. (**c**) ZVS operation equivalent circuit of S_1.

During a switching cycle, the inductor current operates in multiple stages. Due to the symmetry of the two bridges, in Figure 4a, the shaded areas a_1 and a_2 are equal. Therefore, the operating modes of the inductor current in multiple stages can be equivalent to the red dashed line. Taking i_{L1} as an example ($D < 0.5$), the peak-to-peak value of inductor current can be calculated as

$$I_{pp} = \frac{(V_i - V_o)D}{L_{eq1} \cdot f_s} \tag{10}$$

According to the ZVS condition, the switching frequency range can be derived as

$$\begin{array}{l} I_{pp} > 2 \cdot I_{ave} \\ \Rightarrow f_s < \frac{(V_i - V_o)V_o}{2 \cdot L_{eq1} \cdot I_{ave} \cdot V_i} \end{array} \tag{11}$$

where I_{ave} is equal to $I_o/2$.

Similarly, when $D > 0.5$, the range of switching frequency can be expressed as

$$f_s < \frac{(V_i - V_o)V_o}{2 \cdot L_{eq3} \cdot I_{ave} \cdot V_i} \tag{12}$$

When the switching frequency is too low, although ZVS can be achieved, higher circulating currents will be generated. Therefore, the switching frequency is typically set near its upper limit. Combining (11) and (12), the calculation of switching frequency requires consideration of the correct equivalent inductance value at different duty cycles, which can be expressed as

$$\begin{array}{l} f_s = \frac{(V_i - V_o)V_o}{2 \cdot L_{eq} \cdot I_{ave} \cdot V_i} \\ \begin{cases} L_{eq} = L_{eq1} & (D \leq 0.5) \\ L_{eq} = L_{eq3} & (D \geq 0.5) \end{cases} \end{array} \tag{13}$$

2.4. Digital BCM Control Strategy

In this paper, the traditional average current control can be adopted, hence, I_{ave}, V_{in} and V_o need to be sampled by the digital processor. In addition, I_{ave} can be obtained by sampling inductor current at the duty cycle midpoint. The detailed steps are shown in Figure 5. The proposed variable frequency control mainly consists of the following five steps:

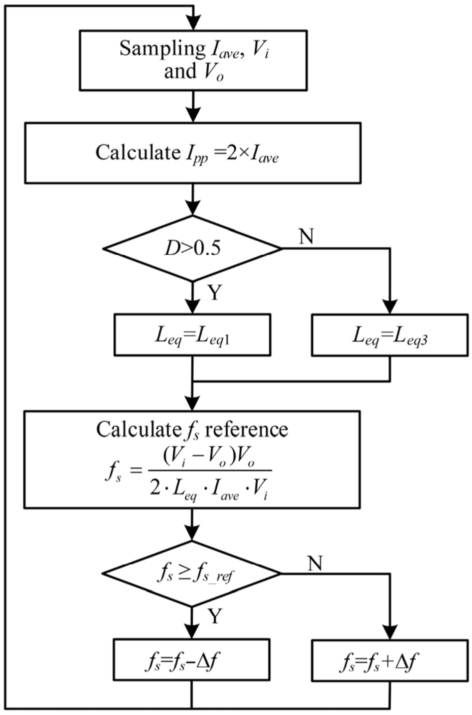

Figure 5. The flow chart of variable frequency control.

Step 1: Sample the average value of inductor current I_{ave}, input voltage V_i and output voltage V_o.

Step 2: Calculate I_{pp}.

Step 3: Determine L_{eq} value.

Step 4: Calculate the switching frequency reference by (13).

Step 5: Adjust the switch frequency.

3. Coupled Inductor Design

3.1. Optimal Coupling Coefficient Design

According to (13), under BCM control, as the operating voltage (duty cycle) varies widely, the switching frequency will also be adjusted widely. It will bring challenges to the design of magnetic components and driving circuits. Among them, the equivalent inductance value L_{eq} will also change with the duty cycle, hence the range of switching frequency can be minimized by designing the optimal coupling coefficient.

Substitute the expression of L_{eq} into (13), which can be rewritten as

$$f_s = \begin{cases} \frac{V_o^2}{P_o(1-\alpha^2)L}(1-D+\alpha D) & D \leq 0.5 \\ \frac{V_o^2}{P_o(1-\alpha^2)L}\frac{(D+\alpha-\alpha D)(1-D)}{D} & D \geq 0.5 \end{cases} \tag{14}$$

where P_o is the entire output power of the two phases.

Equation (14) shows that the switching frequency is inversely proportional to the out-put power. At full load, the switching frequency is the lowest, which is also the most difficult to achieve ZVS. Therefore, it is necessary to design parameters under full load.

Under full load, when the output voltage V_o and self-inductance L are fixed, the switching frequency needs to be adjusted with the duty cycle D. The purpose of designing the optimal coupling coefficient is to minimize the switching frequency range variation with duty cycle. By setting $V_o^2/(P_o \times L)$ to 1, the normalized switching frequency f_{sn} can be obtained as

$$f_{sn} = \begin{cases} \frac{1}{(1-\alpha^2)}(1 - D + \alpha D) & D \leq 0.5 \\ \frac{1}{(1-\alpha^2)}\frac{(D+\alpha-\alpha D)(1-D)}{D} & D \geq 0.5 \end{cases} \quad (15)$$

Base on (15), the relationship between D and the normalized switching frequency f_{sn} under different coupling coefficients α is shown in Figure 6.

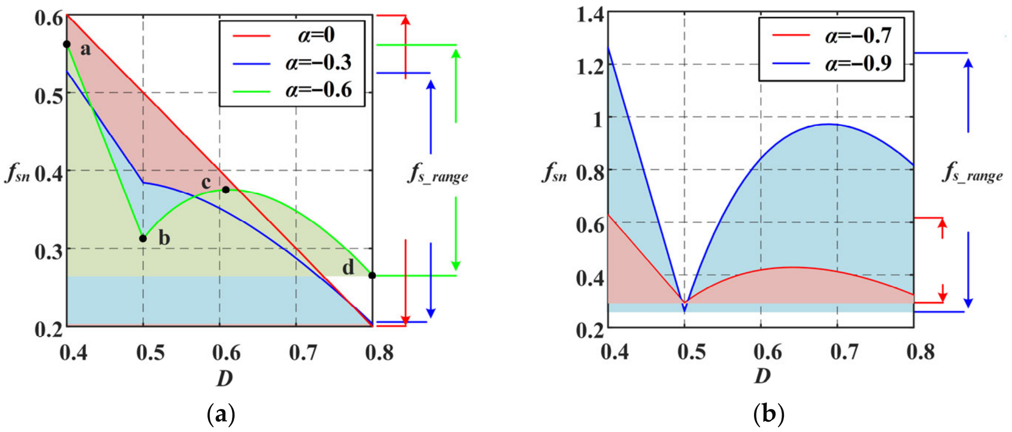

Figure 6. Normalized switching frequency under different coupling coefficients and duty cycles. (**a**) α = 0, α = −0.3 and α = −0.6. (**b**) α = −0.7 and α = −0.9.

When D < 0.5, the $D - f_s$ curve is a monotonically decreasing function. Therefore, the switching frequency of point a (D_{min}) must be greater than that of point b (D = 0.5).

When D > 0.5, the $D - f_s$ curve has a maximum at point c (f'_{sn} = 0). And it also has another boundary value at point d (D_{max}).

To sum up, the highest frequency may occur at point a (D_{min}) or point c (f'_{sn} = 0), and the lowest frequency may occur at point b (D = 0.5) or point d (D_{max}). Taking the experimental prototype built in this paper as an example, the duty cycle range is approximately 0.4~0.8.

The flowchart for designing the optimal coupling coefficient is shown in Figure 7. Firstly, based on the piecewise function (15), the switching frequency points (a, b, c, d) need to be solved. Secondly, calculate the values of four points (a, b, c, d) and determine the highest and lowest frequencies. Thirdly, the frequency range expression can be obtained by subtracting the lowest frequency from the highest frequency. Finally, calculate the coupling coefficient at the lowest frequency range.

The duty cycle range in this paper is 0.4–0.8. Taking this as an example, the optimal coupling coefficient can be calculated through the following four steps.

(1) *Calculate frequency value: The switching frequency of the four points can be calculated as*

$$\begin{cases} f_{sna}|_{D=0.4} = \frac{2\,\alpha+3}{5(1-\alpha^2)} \\ f_{snb}|_{D=0.5} = \frac{\alpha+1}{2(1-\alpha^2)} \\ f_{snc}\Big|_{D=\sqrt{\frac{\alpha}{\alpha-1}}} = \frac{\alpha\,+1}{(1-\alpha^2)}\sqrt{\frac{\alpha}{\alpha-1}} \\ f_{snd}|_{D=0.8} = \frac{\alpha+4}{0.8(1-\alpha^2)} \end{cases} \quad (16)$$

(2) *Determine the maximum and minimum values of switch frequency:* f_{sna} is always greater than f_{snc}; therefore, the maximum switching frequency is equal to f_{sna}. In addition, when $\alpha \leq -2/3$, $f_{snb} < f_{snd}$, and when $\alpha > -2/3$, $f_{snb} > f_{snd}$. Therefore, the maximum and minimum values of the switching frequency can be expressed as:

$$\begin{cases} f_{sn\max} = \frac{2\,\alpha+3}{5(1-\alpha^2)} \\ f_{sn\min} = \begin{cases} \frac{\alpha+1}{2(1-\alpha^2)} & (\alpha \le -2/3) \\ \frac{\alpha+4}{0.8(1-\alpha^2)} & (\alpha > -2/3) \end{cases} \end{cases} \tag{17}$$

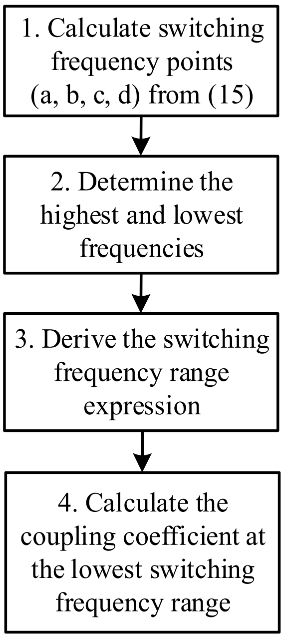

Figure 7. Design flowchart.

(3) *Derive frequency range expression:* After subtracting the minimum value from the maximum value, the range of switching frequency can be derived as

$$f_{srange} = f_{s\max} - f_{s\min} = \begin{cases} \frac{2\,\alpha+3}{5(1-\alpha^2)} - \frac{\alpha+1}{2(1-\alpha^2)} & \alpha \le -2/3 \\ \frac{2\,\alpha+3}{5(1-\alpha^2)} - \frac{\alpha+4}{0.8(1-\alpha^2)} & \alpha > -2/3 \end{cases} \tag{18}$$

(4) *Calculate the optimal coupling coefficient:* According to (16), the relationship between coupling coefficient and switching frequency range is shown in Figure 8. It can be seen that when the coupling coefficient α is approximately -0.6, the range of switching frequencies is minimal. Especially compared with separate inductor designs (α = 0), the adjustment range of switching frequency is significantly reduced. In addition, when the coupling coefficient is around 0.6, the slope of the frequency range function is nearly flat. Even considering a 10% design error, the range of switching frequency variation is very low.

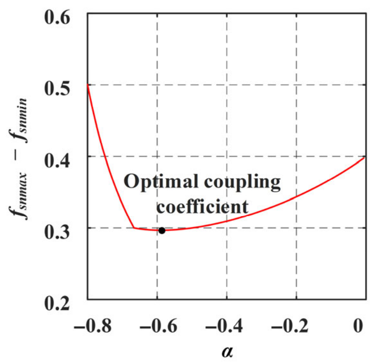

Figure 8. The relationship between coupling coefficient and switching frequency range.

3.2. Self-Inductance Design

According to (13), after determining the coupling coefficient, at full load and lowest switching frequency, the self-inductance range can be expressed as

$$\begin{array}{l} L_{eq} \leq \frac{(V_i - V_o)V_o}{2 \cdot f_s \cdot I_{ave} \cdot V_i} \\ \begin{cases} L_{eq} = L_{eq1} & (D \leq 0.5) \\ L_{eq} = L_{eq3} & (D \geq 0.5) \end{cases} \end{array} \tag{19}$$

Based on (19), the self-inductance range is shown in Figure 9. Below the red curve is the ZVS area. In addition, a too low inductance value can lead to a higher circulating current, hence the self-inductance value needs to be designed near the upper boundary value. In this paper, the self-inductance value is designed to be about 10 μH.

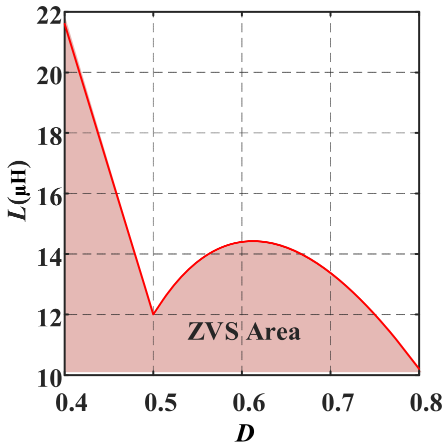

Figure 9. Range of self-inductance values.

3.3. Coupled Inductor Structure Design

In order to increase the coupling degree between the primary and secondary sides, a coupled inductor with interleaved winding structure is adopted in this paper, as shown in Figure 10a. The two windings are wound on the outer side leg of the magnetic core. The total turns are (N_m + N_c). Taking winding L_1 as an example, on the left leg, the number of turns in the main winding is N_m. On the right leg, the number of turns crossing with winding L_2 is N_c. Due to the symmetry of the coupled inductor structure, winding L_2 has a similar distribution. The air gap length of both outer legs is l_{go}, and the air gap length of the central leg is l_{go}. In addition, the cross-sectional areas of the outer leg and the central leg are A_{eo} and A_{ec}, respectively.

According to the structure of the winding, the equivalent magnetic circuit is shown in Figure 10b. The magnetic flux of the outer leg is ϕ_1 and ϕ_2, respectively. The magnetic flux of the central leg is ϕ_c. The magnetic resistance of the outer leg and the central leg are R_{go} and R_{gc}, respectively. According to the superposition theorem, ϕ_1, ϕ_2 and ϕ_c can be calculated as

$$\begin{cases} \phi_1 = \frac{N_m I_1 - N_c I_2}{R_{go} + \frac{1}{\frac{1}{R_{go}} + \frac{1}{R_{gc}}}} + \frac{N_c I_1 - N_m I_2}{R_{go} + \frac{1}{\frac{1}{R_{go}} + \frac{1}{R_{gc}}}} \cdot \frac{R_{gc}}{R_{go} + R_{gc}} \\ \phi_2 = \frac{N_m I_2 - N_c I_1}{R_{go} + \frac{1}{\frac{1}{R_{go}} + \frac{1}{R_{gc}}}} + \frac{N_c I_2 - N_m I_1}{R_{go} + \frac{1}{\frac{1}{R_{go}} + \frac{1}{R_{gc}}}} \cdot \frac{R_{gc}}{R_{go} + R_{gc}} \\ \phi_c = \phi_1 + \phi_2 \end{cases} \tag{20}$$

According to the definition, self-inductance and mutual inductance can be expressed as

$$\begin{cases} L = \left.\frac{N_m\phi_1 - N_c\phi_2}{I_1}\right|_{I_2=0} \\ = \frac{(N_m^2+N_c^2)R_{go}+(N_m+N_c)^2R_{gc}}{R_{go}(R_{go}+2R_{gc})} \\ M = \left.\frac{N_m\phi_1 - N_c\phi_2}{I_2}\right|_{I_1=0} \\ = -\frac{(N_m^2+N_c^2)R_{gc}+2N_mN_c(R_{go}+R_{gc})}{R_{go}(R_{go}+2R_{gc})} \end{cases} \tag{21}$$

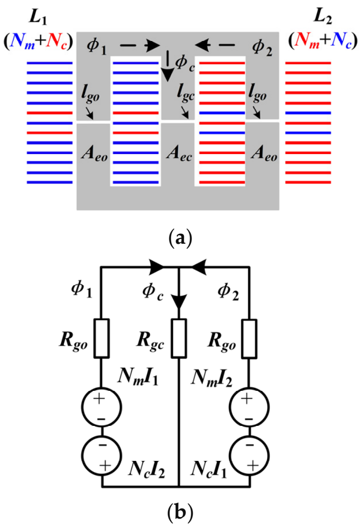

Figure 10. Coupled inductor structure. (**a**) Coupled inductor with interleaved winding structure. (**b**) Equivalent magnetic circuit.

After the self-inductance, mutual-inductance, and number of turns are determined, the magnetic reluctance R_{go} and R_{gc} can be solved. Then, based on the relationship between air gap and magnetic resistance, the air gap length can be calculated as

$$\begin{cases} l_{go} = R_{go}\mu_0 A_{eo} \\ l_{gc} = R_{gc}\mu_0 A_{ec} \end{cases} \tag{22}$$

In this paper, the magnetic core type EE4220 is adopted. The main winding turns number N_m is 11, and the crossing winding turns number N_c is 2. The outer leg and the center leg air gap length are both approximately 1.5 mm. According to the design parameters, the waveforms of magnetic flux density and current are shown in Figure 11. The magnetic flux density peak to peak value can be deduced as $(B_{max} - B_{min})/2$. In addition, in the proposed coupled inductor structure, the magnetic flux density of the center leg is reduced due to the 180 degree phase difference of the inductor current. But the magnetic flux density of the outer leg is higher.

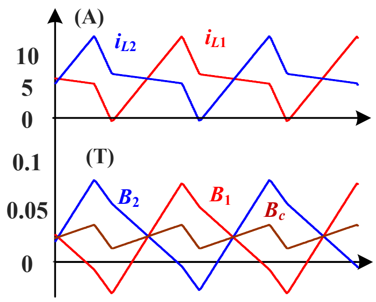

Figure 11. Magnetic flux density waveforms.

3.4. ZVS Range

In this paper, the lowest frequency is 50 kHz, with a duty cycle range of approximately 0.4–0.8 (input voltage 30–60 V, output voltage 24 V). The ZVS range figures at the rated power (300 W) and 1.5 times overload (450 W) are shown in Figure 12. According to ZVS analysis, $I_{ave} - I_{pp}/2$ needs to be less than zero to achieve ZVS. Under the rated power (300 W), ZVS can be implemented when the duty cycle is less than 0.8. When the duty cycle is greater than 0.8, ZVS will be lost. In addition, at higher power,, such as 1.5 times overload (450 W), ZVS can only be implemented when the duty cycle is less than 0.45. Hence, ZVS is more difficult to achieve at high power.

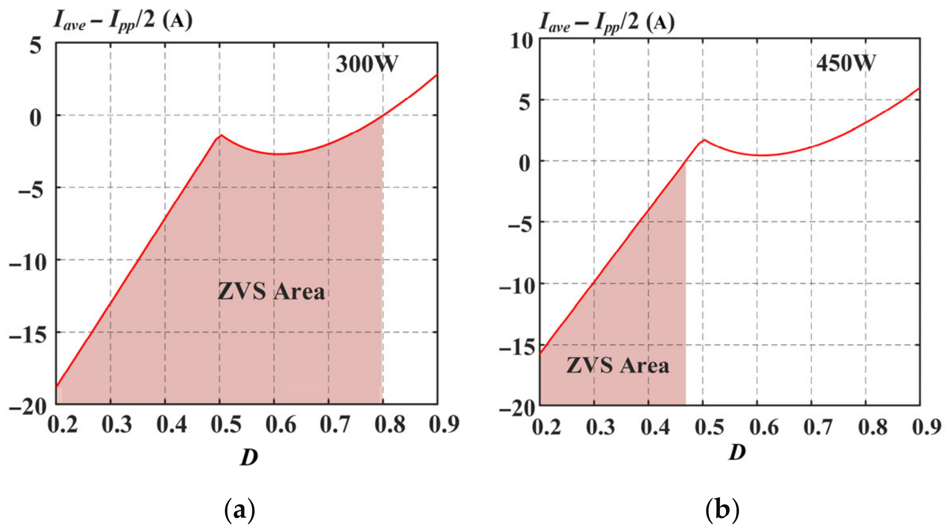

Figure 12. ZVS range. (**a**) 300 W. (**b**) 450 W.

3.5. Characteristic Comparison

Under the same parameters of voltage range, operating power, and minimum switching frequency, a comparison is conducted among the following three types of Buck converters with different inductors: separate inductors, positively coupled inductors (α = 0.6), and negatively coupled inductors ($\alpha = -0.6$).

The simulation waveforms of the negatively coupled inductor and the separate inductor are shown in Figure 13. In addition, the detailed comparative data are shown in Table 2. Regarding current ripple, under the control of the BCM, in order to achieve ZVS, the peak-to-peak value of the inductor current in each phase is approximately equal to twice the average value. Therefore, the three types of current ripple and circulating current are completely identical. However, in order to achieve BCM control, the switching frequency ranges are different. The negatively coupled inductor with the optimal coupling coefficient has the narrowest frequency range, as shown in Figure 14. Furthermore, for dynamic equivalent inductance ($L(1+\alpha)$, as shown in Table 1), using positively coupled inductor will increase the equivalent inductance. Therefore, dynamic response is decreased.

Table 2. Characteristic comparison.

	Separate Inductors	Positively Coupled Inductors (α = 0.6)	Negatively Coupled Inductors ($\alpha = -0.6$)
Current ripple	equal	equal	equal
Frequency range	medium	wide	narrow
Dynamic response	-	decrease	increase

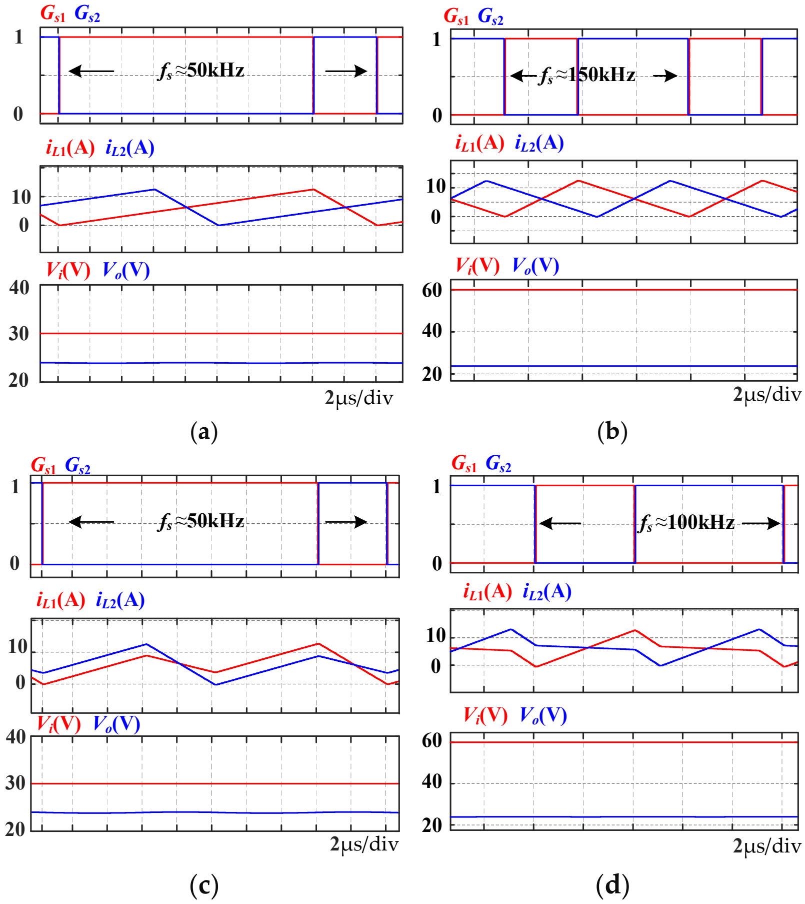

Figure 13. Simulation waveforms (300 W). (**a**) Separate inductor, 30 V. (**b**) Separate inductor, 60 V. (**c**) Coupled inductor, 30 V. (**d**) Coupled inductor, 60 V.

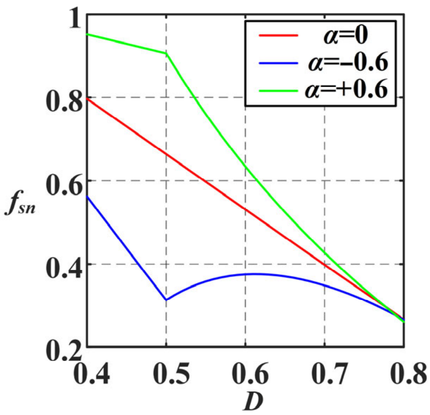

Figure 14. Switching frequency range.

3.6. Loss Analysis and Comparison

The theoretical loss analysis results are shown in Figure 15. All MOSFETs can achieve ZVS; therefore, the turning-on loss of MOSFETs can be ignored. The main losses include turning-off loss, conduction loss, core loss and copper loss. The loss analysis results are compared with the separate-inductor converter. Among them, the separate inductors are designed with two EE30 magnetic cores. The overall cost is similar to that of one EE4220 magnetic core. Due to the adoption of the optimal coupling coefficient design, the switching frequency range is narrower, and the proposed converter can achieve BCM at lower frequency. Therefore, the turning off losses and core losses are lower than in the case with the separate-inductor converter, and the overall efficiency of the proposed converter is also higher.

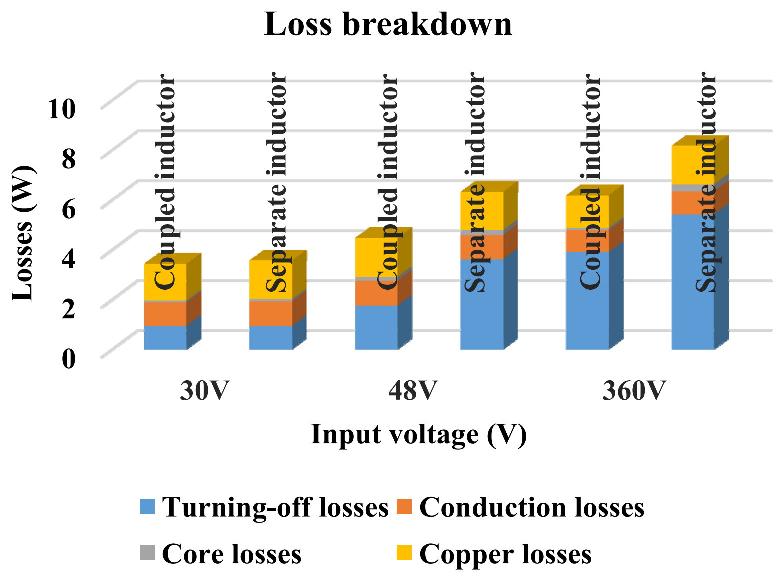

Figure 15. Loss analysis.

In addition, the main losses of the converter are conduction loss and turn-off loss. This is because under BCM control, the peak-to-peak value of the inductor current is relatively high (twice the average value). Therefore, the proposed solution is more suitable for low-current applications.

4. Experimental Verification

In order to validate the performance of optimal design with the coupling coefficient, an experimental prototype is built. The detailed parameters are listed in Table 3.

Table 3. Parameters of the Experimental Prototype.

Designed Parameters	Value
Input voltage (V_{in})	30–60 V
Output voltage (V_o)	24 V
Rated power (P_o)	300 W
Self-inductance (L)	10 µH
Coupling coefficient (α)	−0.6
Switching frequency (f_s)	50–200 kHz

The full load steady-state operating waveforms with different loads and input voltages are shown in Figure 16. It can be seen that the phase difference between the two-phase inductor currents is 180 degrees. And the inductor current has multiple stages within one switching cycle, which is consistent with theoretical analysis. Under BCM control, the inductor current valley value is slightly below zero. The drain-source voltage of MOSFET has already dropped to zero before turning on, hence ZVS can be achieved. In addition, the switching frequency will be adjusted at different voltages to achieve BCM operation. Therefore, the valley value of inductor current is relatively fixed. Under the optimal coupling coefficient design, the lowest switching frequency is approximately 50 kHz (V_i = 30 V) and the highest switching frequency is approximately 100 kHz (V_i = 60 V). The experimental results are consistent with the simulation results in Figure 13. Under the proposed optimization design, the switching frequency range is relatively narrow when operating at full load.

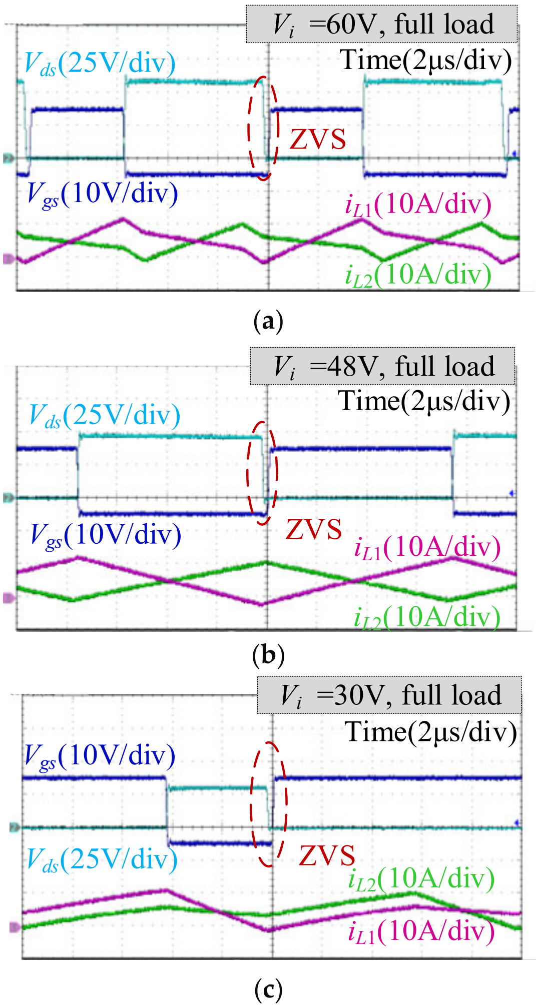

Figure 16. Full-load steady-state waveforms. (**a**) Input 60 V. (**b**) Input 48 V. (**c**) Input 30 V.

The experimental waveforms of half-load operation are shown in Figure 17. Because the average value of inductor current decreases, the switching frequency needs to be increased. In this way, while maintaining ZVS operation, the ripple of inductor current is reduced to decrease conduction loss.

The waveform of the no-load experiment is shown in Figure 18. It can be seen that under no-load conditions, ZVS is very easy to be achieved because the average value of inductor current is close to zero. In order to reduce the circulating current, the switching frequency will be adjusted to the highest level (200 kHz).

The dynamic waveforms are shown in Figures 19 and 20. Under digital BCM control, adjusting the switching frequency will cause the inductor current to enter a transient state. In order to prevent frequency adjustment from disturbing the voltage and current control loops, the switching frequency is adjusted using a ramp function. In this paper, the control and sampling periods are both 20 kHz. In addition, the adjustment step of the switching frequency is 0.1 kHz. When the load switches from full load to half load, the switching frequency is increased to reduce the circulating current. Similarly, when the load is increased, the switching frequency will be reduced to achieve ZVS. The adjustment time for current ripple and switching frequency is approximately 20 ms. When the input voltage changes, the switching frequency also needs to be adjusted, and the ripple of the inductor current remains constant.

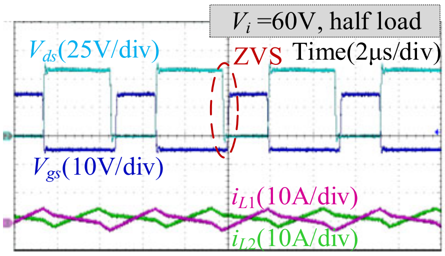

(**a**)

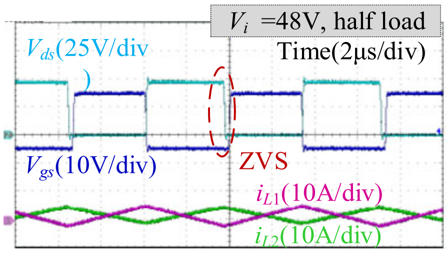

(**b**)

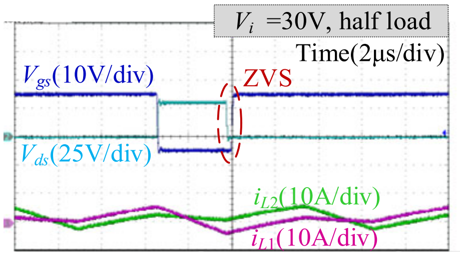

(**c**)

Figure 17. Half-load steady-state waveforms. (**a**) Input 60 V. (**b**) Input 48 V. (**c**) Input 30 V.

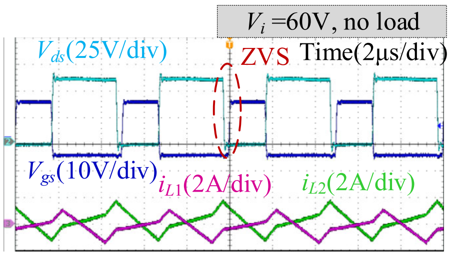

(**a**)

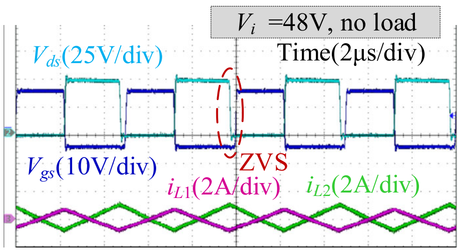

(**b**)

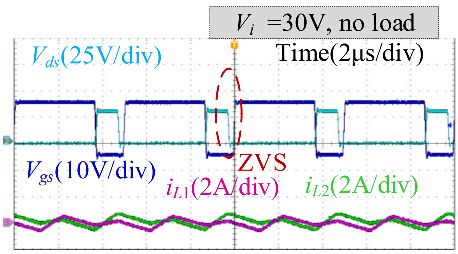

(**c**)

Figure 18. No-load steady-state waveforms. (**a**) Input 60 V. (**b**) Input 48 V. (**c**) Input 30 V.

The measurement efficiency curves are shown in Figure 21. At low input voltages, the switching frequency is correspondingly reduced, resulting in lower turn-off losses and core losses. Conversely, under high input voltages, an increased switching frequency is required to reduce current ripple, which leads to relatively higher turn-off and core losses. Overall, the operating efficiency of the converter is higher at low input voltages.

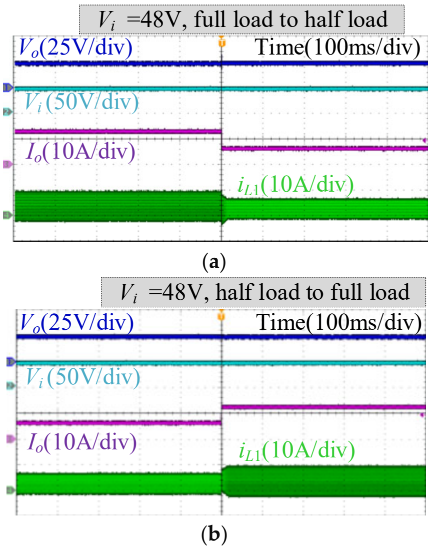

Figure 19. Load-switching waveforms. (**a**) Full load to half load. (**b**) Half load to full load.

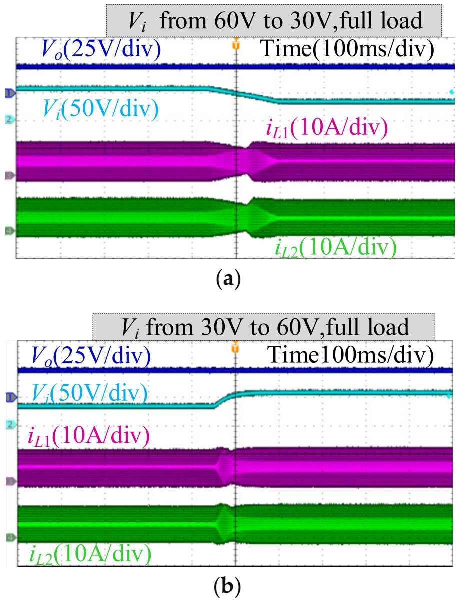

Figure 20. Input voltage switching waveforms. (**a**) 60 V to 30 V. (**b**) 30 V to 60 V.

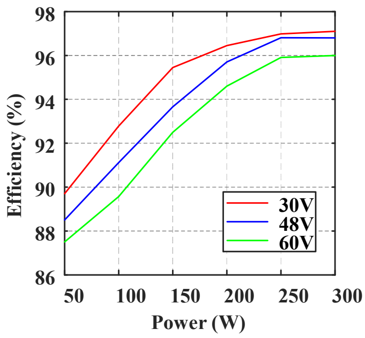

Figure 21. Measurement efficiency.

5. Conclusions

In this paper, an interleaved Buck converter with negatively coupled inductor and optimal coupling coefficient is proposed. The proposed converter operates under BCM to achieve ZVS. A fully digital adaptive frequency control strategy is implemented, eliminating the need for ZCD circuits or auxiliary components. Compared with the analog scheme, the proposed method only requires sampling the average values of voltage and current, which can reduce the sensitivity to sampling noise. In addition, in order to reduce the adjustment range of the switching frequency, a design method for the optimal coupling coefficient is proposed. Compared with separate-inductor designs, the adjustment range of switching frequency is significantly reduced. A 300 W experimental prototype was built, and the experimental results validated the effectiveness of the proposed solution.

Author Contributions: Conceptualization, J.X., X.C. and X.H.; methodology, J.X. and X.C.; writing—original draft preparation, J.X. and X.C.; writing—review and editing, J.X. and X.H. All authors have read and agreed to the published version of the manuscript.

Funding: This work was supported in part by the National Natural Science Foundation of China under Grant 52407232, 52307232, Key Research and Development Program of Hunan Province under Grant 2024JK2013, the Hunan Provincial Natural Science Foundation of China under Grant 2026JJ60192, 2024JJ4055, and the State Key Laboratory of Power System Operation and Control under Grant SKLD23KM12.

Data Availability Statement: The original contributions presented in the study are included in the paper. Further inquiries can be directed to the corresponding author.

Conflicts of Interest: The authors declare no conflicts of interest.

Nomenclature

V_i, V_o	Input voltage and output voltage
P_o	Output power
L_1, L_2	Self-inductance
M	Mutual inductance
α	Coupling coefficient
v_{L1}, v_{L2}	Terminal voltage of coupled inductor windings L_1 and L_2
i_{L1}, i_{L2}	Current of coupled inductor windings L_1 and L_2
D	Duty cycle of S_1 and S_3
I_{pp}	Peak to peak value of inductor current
I_{ave}	Average value of inductor current
f_{sn}	Normalized switching frequency
N_m	Main winding turns number
N_c	Crossing turns number
l_{go}, l_{gc}	Air gap length of outer legs and central leg
A_{eo}, A_{ec}	Cross-sectional areas of outer leg and central leg
ϕ_1, ϕ_2, ϕ_c	Magnetic flux of the outer leg and central leg

References

1. Jia, X.; Sha, D.; Zhao, Y. Unified One-Cycle Control for Fully Digitalized ZVS Four-Switch Buck–Boost Converter During Bidirectional Power Flow Transition. *IEEE Trans. Power Electron.* **2024**, *39*, 11295–11307. [CrossRef]
2. Abdurraqeeb, A.M.; Al-Shamma'a, A.A.; Alkuhayli, A.; Noman, A.M.; Addoweesh, K.E. RST Digital Robust Control for DC/DC Buck Converter Feeding Constant Power Load. *Mathematics* **2022**, *10*, 1782. [CrossRef]
3. Zhao, Z.; Luo, P.; Zhang, Z.; Fan, J.; Zhang, B.; Chen, X. A Peak-Valley Current-Mode Buck Converter With 3% to 95% Duty Cycle. *IEEE Trans. Circuits Syst. II Express Briefs* **2025**, *72*, 328–332. [CrossRef]
4. Zambrano-Gutierrez, D.F.; Cruz-Duarte, J.M.; Castañeda, H.; Avina-Cervantes, J.G. Optimization of Adaptive Sliding Mode Controllers Using Customized Metaheuristics in DC-DC Buck-Boost Converters. *Mathematics* **2024**, *12*, 3709. [CrossRef]

5. Zhang, J.; Li, Y.; Wan, J.; Zhao, B.; Zhang, Y.; Liu, F. A New Active Clamp Zero-Voltage-Transition Cell for Non-Isolated DC-DC Converter with Low Current Stress. *CPSS Trans. Power Electron. Appl.* **2025**, *10*, 231–240. [CrossRef]
6. Mohammadi, M.R. An active-clamping ZVS interleaved buck/boost bi-directional converter with one auxiliary switch. *IEEE Trans. Ind. Electron.* **2020**, *67*, 7430–7438. [CrossRef]
7. Pal, A.; Saha, S.S. Novel Zero-Voltage Zero-Current Transition Buck Converter With Minimal Impact of Active Auxiliary Cell on Overall Dynamics. *IEEE Access* **2023**, *11*, 3008–3023. [CrossRef]
8. Dago, A.; Leoncini, M.; Saggini, S.; Brunero, A.; Gasparini, A.; Zambetti, O.; Levantino, S.; Ghioni, M. A High-Power-Density Quasi-Resonant Switched-Capacitor DC–DC Converter With Single Semiperiod Tank Current Modulation. *IEEE Trans. Power Electron.* **2024**, *39*, 2100–2114. [CrossRef]
9. Kong, I.-B.; Kim, W.-S.; Lee, S.-W. A Novel High-Voltage-Gain Quasi-Resonant DC–DC Converter With Active-Clamp and Switched-Capacitor Techniques. *IEEE Trans. Power Electron.* **2023**, *38*, 7810–7820. [CrossRef]
10. Hinov, N.; Gilev, B. Neural Network-Based Design of a Buck Zero-Voltage-Switching Quasi-Resonant DC–DC Converter. *Mathematics* **2024**, *12*, 3305. [CrossRef]
11. Hinov, N.; Gilev, B. Comparison of Different Optimization Techniques for Model-Based Design of a Buck Zero Voltage Switching Quasi-Resonant Direct Current to Direct Current Converter. *Mathematics* **2023**, *11*, 4990. [CrossRef]
12. Huang, X.; Lee, F.C.; Li, Q.; Du, W. High-Frequency High-Efficiency GaN-Based Interleaved CRM Bidirectional Buck/Boost Converter with Inverse Coupled Inductor. *IEEE Trans. Power Electron.* **2016**, *31*, 4343–4352. [CrossRef]
13. Tang, Y.; Zhang, C.; Guo, Y.; Sun, H.; Jiang, L. Optimization of Minimum Negative Current BCM Synchronous Buck Converter. *IEEE Trans. Ind. Electron.* **2023**, *70*, 9677–9684. [CrossRef]
14. Michal, V. Inductor Current Zero-Crossing Detector and CCM/DCM Boundary Detector for Integrated High-Current Switched-Mode DC–DC Converters. *IEEE Trans. Power Electron.* **2014**, *29*, 5384–5391. [CrossRef]
15. Shi, Y.; Liu, X.; Li, X.; Wang, S.; Peng, L.; Zhou, Z.; Zhang, B. An Ultra-Low Quiescent Current Adaptive ZCD Technique for Discontinuous-Conduction-Mode Control Applications. *IEEE Trans. Circuits Syst. II Express Briefs* **2025**, *72*, 1635–1639. [CrossRef]
16. Baek, J.; Choi, W.; Cho, B. Digital adaptive frequency modulation for bidirectional DC-DC converter. *IEEE Trans. Ind. Electron.* **2013**, *60*, 5167. [CrossRef]
17. Sankaranarayanan, V.; Gao, Y.; Erickson, R.W.; Maksimovic, D. Online Efficiency Optimization of a Closed-Loop Controlled SiC-Based Bidirectional Boost Converter. *IEEE Trans. Power Electron.* **2022**, *37*, 4008–4021. [CrossRef]
18. Liu, Y.-C.; Syu, Y.-L.; Dung, N.A.; Chen, C.; Chen, K.-D.; Kim, K.A. High-Switching-Frequency TCM Digital Control for Bidirectional-Interleaved Buck Converters Without Phase Error for Battery Charging. *IEEE J. Emerg. Sel. Top. Power Electron.* **2020**, *8*, 2111–2123.
19. Meng, Z.; Zhao, K.; Wang, S.; Sun, L. A Soft-Switching Method for Interleaved Buck Converter Based on Variable-Frequency Peak Current Control. *IEEE Trans. Ind. Electron.* **2025**, 1–13. [CrossRef]
20. Mayer, R.; El Kattel, M.B.; Oliveira, S.V.G. Multiphase Interleaved Bidirectional DC/DC Converter With Coupled Inductor for Electrified-Vehicle Applications. *IEEE Trans. Power Electron.* **2021**, *36*, 2533–2547. [CrossRef]
21. Huang, W.; Lehman, B. A Compact Coupled Inductor for Interleaved Multiphase DC–DC Converters. *IEEE Trans. Power Electron.* **2016**, *31*, 6770–6775. [CrossRef]
22. Pajnić, M.; Pejović, P. Zero-Voltage Switching Control of an Interleaved Bi-Directional Buck–Boost Converter With Variable Coupled Inductor. *IEEE Trans. Power Electron.* **2019**, *34*, 9562–9572. [CrossRef]
23. Wong, P.-L.; Xu, P.; Yang, P.; Lee, F. Performance improvements of interleaving VRMs with coupling inductors. *IEEE Trans. Power Electron.* **2001**, *16*, 499–507. [CrossRef]